Pressure-induced dislocations and their influence on ionic transport in Li⁺ conducting argyrodites

Vasiliki Faka,^a Matthias T. Agne,^a Martin A. Lange,^a Dominik Daisenberger,^b Björn Wankmiller,^{a,c,d} Stefan Schwarzmüller,^e Hubert Huppertz,^e Oliver Maus,^{a,d} Bianca Helm,^a Thorben Böger,^{a,d} Johannes Hartel,^a Josef Maximilian Gerdes,^c Jamie J. Molaison,^f Gregor Kieslich,^g Michael Ryan Hansen,^{c,d} Wolfgang G. Zeier*^{a,d,h}

^aInstitute of Inorganic and Analytical Chemistry, University of Münster, Corrensstraße 28/30, 48149 Münster, Germany.

^bDiamond Light Source, Harwell Science and Innovation Campus, Didcot, Oxfordshire
OX11 ODE, UK.

constitute of Physical Chemistry, University of Münster, Corrensstraße 28/30, 48149

Münster, Germany.

^dInternational Graduate School BACCARA, Wilhelm-Schickard-Straße 8, 48149

Münster, Germany.

^eInstitute of General, Inorganic and Theoretical Chemistry, University of Innsbruck,
Innrain 80/82, 6020 Innsbruck, Austria.

fNeutron Scattering Division, Institute Oak Ridge National Laboratory (ORNL), Oak
Ridge, Tennessee 37831-6473, United States.

^gTechnical University of Munich, TUM School of Natural Sciences, Department of Chemistry, Lichtenbergstraße 4, 85748 Garching, Germany.

hInstitut für Energie- und Klimaforschung (IEK), IEK-12: Helmholtz-Institut Münster,
Forschungszentrum Jülich, 48149 Münster, Germany.

E-mail:

^{*}wzeier@uni-muenster.de

ABSTRACT

The influence of microstructure on ionic conductivity and cell performance is a topic of broad scientific interest in solid-state batteries. The current understanding is that interfacial decomposition reactions during cycling induce local strain at the interfaces between solid electrolytes and anode/cathode, as well as within the electrode composites. Characterizing the effects of internal strain on ion transport is particularly important given the significant local chemomechanical effects caused by volumetric changes of the active materials during cycling. Here, we show the effects of internal strain on the bulk ionic transport of the argyrodite Li₆PS₅Br. Internal strain is reproducibly induced by applying pressures with values up to 10 GPa. An internal permanent strain is observed in the material indicating long-range strain fields typical for dislocations. With increasing dislocation densities, an increase in the lithium ionic conductivity can be observed that extends into an improved ionic transport in solid-state battery electrode composites. This work shows the potential of strain engineering as an additional approach for tuning ion conductors without changing the composition of the material itself.

KEYWORDS

Strain engineering, dislocation densities, pressure, solid electrolytes, argyrodites.

INTRODUCTION

Solid-state batteries using inorganic ion conductors are considered to be one of the most promising next-generation technologies for energy storage. To achieve successful commercialization, the development of batteries with higher energy densities and better cycling performance at affordable cost is indispensable.^{1,2} Many solid electrolytes have been synthesized in the past years and much effort has been made on structural modifications to achieve faster ion transport.³ Even within the same class of materials, there is a large variation of the ionic conductivity achieved by modifications in composition and disorder.^{4,5} Lattice softness, polarizability and the energy landscape are tunable factors which reveal the enormous influence of the structural changes on ion transport.^{6,7} Lithium argyrodites Li_6PS_5X (X = Cl, Br, I) have attracted considerable interest as electrolytes for solid-state batteries due to their intrinsically high ionic conductivities and their structural tunability, which make even higher ionic conductivities achievable. Typically, lithium argyrodites are synthesized by solid-state synthesis or ball milling.^{8,9} Interestingly, the cooling process results in tunable Br/S-site disorders which affect the ionic conductivities in Li₆PS₅Br.^{5,10} In addition, elemental substitutions have been proposed to lower the activation energy and flatten the energy landscapes for Li⁺ transport, ^{4,11} as well as tune the charge carrier density, 12 possibly leading to enhanced ionic conductivities. Nevertheless, it still remains challenging to significantly increase the ionic conductivity of these materials to achieve higher performance in solid-state batteries.⁶

Theoretically, strain has been suggested to potentially affect the ionic conductivity in solids, ¹³ however, strain engineering has yet to be explored in the fast conducting solid electrolytes for solid-state batteries. Strain engineering, and more specifically the incorporation of internal strain into materials, has been historically developed to tune mechanical properties, ¹⁴ as well as thermal and electronic transport. ¹⁵ In the analysis of strain, both elastic and plastic deformation need to be considered. For instance, elastic strain is reversible and disappears once the external forces are removed, where the material returns to its original shape. It is governed by Hooke's law and is characterized by a linear stress-strain relationship. In contrast, plastic strain is permanent and arises as a result of introducing dislocations into the atomic structure

(as illustrated in Figure 1b). This introduction of dislocations occurs through macroscopic plastic deformation of the material.¹⁶

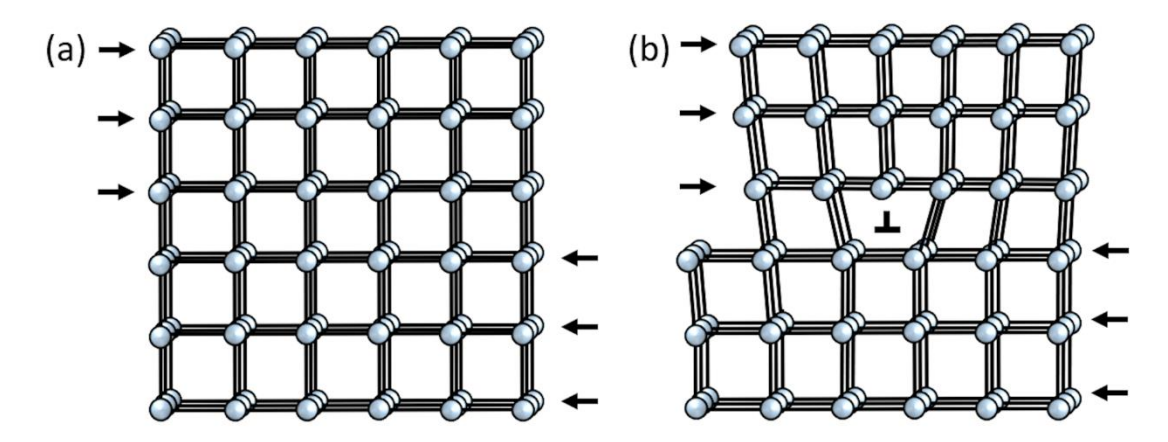


Figure 1. Dislocation in a cubic lattice. (a) A representation of the atomic rearrangements in a cubic pristine lattice, where the arrows represent the applied stress and (b) atomic rearrangements which accompanied by the motion of an edge dislocation as it moves in response to applied stress. The center represents the edge dislocation line.

Dislocations are non-equilibrium defects that are kinetically stable but will annihilate when they become mobile enough at elevated temperatures. Dislocations are characterized by the Burgers vector, which gives information about their orientation and their magnitude. Within the dislocation, a dislocation core is the central region of a dislocation line, at which the lattice structure is distorted or disrupted due to the presence of the dislocation. It is a small, localized region on the atomic level within a crystal lattice with high density of defects and lattice irregularities. Because dislocation cores are topologically one-dimensional, there has been particular interest in using them to tune electronic and ionic transport properties. The intrinsic ability of dislocations to multiply and propagate determines many mechanical properties of metals and alloys. Vacancies and interstitials can rapidly diffuse, by using dislocation cores as pathways/fast diffusion channels. In particular, the open space at the dislocation core offers fast diffusion channels for defects and dislocation lines can act as fast paths for diffusing atoms; a phenomenon called pipe diffusion. 17,18

Elastic strain has been proposed to enhance the performance of electrochemical devices, such as solid oxide fuel cells^{19,20} and batteries²¹ by enhancing ion conduction.

However, it was shown that dislocation cores can have a negative impact on oxide ion diffusion in metal oxides by slowing down the ions because of the segregation of charged defects.¹⁷ As oxygen vacancies and dopant metal cations both accumulate at dislocation cores, these ionic defects can then interact and trap each other.¹⁷ In terms of thermal transport, the introduction of dislocations effectively result in the scattering of the mid-frequency phonons, reducing the lattice thermal conductivity and improving the thermoelectric figure of merit.^{22,23} Strain and microstructural changes at heterophase boundaries in composite solid electrolytes have been suggested to be responsible for the increased ionic conductivity.²⁴ Regarding solid electrolytes for solid-state batteries, strain is present at the interface of the solid electrolyte with the cathode and the anode due to interfacial reactions and volumetric expansion and contraction of the electrodes during charging and discharging cycles. 13 The effects of strain on Li⁺ diffusion have been reported for the β -Li₃PS₄ solid electrolyte by using abinitio molecular dynamics, where elastic strain was suggested to promote Li⁺ disorder and increase ionic conductivity, having a similar effect as chemical substitution.¹³ Although internal strain has also been shown to induce lattice softening, ¹⁶ it is unclear whether it may result in decreased activation barrier for ionic transport. Effects of dislocations have also been studied in yttria-stabilized zirconia used as a solid electrolyte for fuel cells, where their introduction led to higher ionic conductivity.²⁵

Based on these studies, applying stress to a solid can lead to structural changes in materials. In porous materials, while applying pressure initially consolidates a material, it can involve plastic deformation during of the rearrangement of particles. After the material is fully densified, the application of additional pressure will begin to compress the structure itself.²⁶ As electrolytes are usually consolidated at high-pressures of 350 MPa and above,²⁷ and solid-state batteries are still often constructed to have a nominal stack pressure of over 50 MPa,²⁸ there is an open question as to what happens to Li⁺ conductors under these elevated pressures.

In this work, we investigate strain engineering to alter the ionic conductivity of Li_6PS_5Br . Strain is induced in Li_6PS_5Br by applying pressure (0.5 GPa, 1.0 GPa, 1.5 GPa and 10.0 GPa) and characterized using powder X-Ray diffraction. Powder X-ray diffraction analyses of the already pressed/strained material ("ex-situ") are compared to the

synchrotron X-ray diffraction analyses under applied pressure ("in-situ"). The strain is quantified and compared for both techniques, using the Williamson-Hall method and the Stephens' anisotropic strain model. Internal strain remains in the material, even after the release of the applied pressure, corresponding to the introduction of dislocations into the structure. Pair distribution function and Raman analyses reveal no change in the short-range local structure. However, the dislocations shorten the overall coherence length of the material, indicating that the origin of the long-range strain is caused by dislocations. Nuclear magnetic resonance and impedance spectroscopy analyses suggest that the short-range transport is hindered in strained Li₆PS₅Br and that the long-range total ionic transport is improved. Finally, the strained and unstrained Li₆PS₅Br are tested as catholytes in solid-state batteries to examine if the strain is favorable for the electrochemical performance. The ion transport of the composite material is analyzed by measuring the partial ionic and electronic conductivities, as obtained from transmission line modeling of impedance measurements, as well as DC polarization measurements. This work shows the impact of internal strain on the ionic conductivity of solid electrolytes and underlines the significance of an accurate understanding of the processes occurring in solid state batteries under pressure.

METHODS

Synthesis. All synthesis steps of Li₆PS₅Br were carried out under inert Ar atmosphere ($O_2 < 0.5$ ppm and $H_2O < 0.5$ ppm). Lithium sulfide (Li₂S, *Alfa-Aesar*, 99.9%), phosphorous pentasulfide (P_4S_{10} , *Merck*, 99%) and lithium bromide (LiBr, ultradry, *Alfa-Aesar*, 99.99%) were mixed in the appropriate stoichiometric ratio and hand-ground in an agate mortar. For the ball-milling synthesis, the obtained composition was transferred into a 45 mL zirconia ball milling cup with 5 mm diameter balls (40:1 mass ratio of balls to precursor) and milled for a total of 150 cycles (10 minutes milling time and 10 minutes resting time). During the 150 cycles of milling, the ball mill cups were opened twice to remove the caked powder from the walls of the milling cups and to hand-grind it. Subsequently, the obtained powder was pressed into a 1 cm diameter pellet and filled into carbon-coated ampoules that had been preheated at 1073 K for 2 hours under dynamic vacuum to remove any traces of H_2O . The ampoules were then sealed under pressure < 10^{-1} mbar and transferred into a tube furnace already preheated to 823 K. The ampoules filled with material were annealed for 30 minutes and left to cool down with a cooling rate of 4 K/h, resulting in 10% Br⁻/S²⁻ site disorder.⁵

Uniaxial applied pressure experiments for strain introduction and potentiostatic electrochemical impedance spectroscopy (PEIS). A CompreDrive setup (rhd instruments) was used for the pressure-dependent experiments. 100 mg of Li_6PS_5Br was loaded into a 6C CompreCell (6 mm diameter) under Ar atmosphere ($H_2O < 0.5$ ppm and $O_2 < 0.5$ ppm). Pressure was applied uniaxially and kept constant with high accuracy (0.5%) during the entire measurement. An external heating mantle kept the internal temperature of CompreCell constant at T = 298 K, controlled via a Presto A40 thermostat (Julabo). AC impedance spectroscopy was utilized to determine the ionic conductivities and the impedance spectra were recorded with an SP-150 impedance analyzer (Bio-Logic Science instruments Ltd.) at room temperature. The temperature was equilibrated at T = 298 K for two hours, in the beginning of each measurement, to ensure complete stabilization of the pellet temperature. Potentiostatic electrochemical impedance spectroscopy (PEIS) was recorded utilizing a sinusoidal excitation voltage signal of 150 mV in a frequency range from 1 MHz to 100 mHz. The resulting impedance spectra were evaluated with RelaxIS 3 Impedance Spectrum

Analysis software (rhd instruments) and the data quality was examined by using the Kramers-Kronig relations to determine the reliable frequency range for data fitting.

Powder X-Ray Diffraction and Synchrotron High-Pressure Powder X-Ray Diffraction.

Powder X-ray diffraction measurements were performed on a laboratory STOE STADI P diffractometer in Debye-Scherrer geometry with a Dectris MYTHEN2 1K detector in Debye-Scherrer mode at room temperature. The radiation source was Cu Kalpha(1) (λ = 1.5406 Å) employing a Ge(111) monochromator. The X-ray diffraction data was collected within a 2θ range from 10° to 70° in $\Delta(2\theta)$ = 0.015° steps. All samples were

measured in sealed borosilicate glass capillaries with a diameter of 0.5 mm to ensure

no reaction with air and moisture.

Synchrotron high-pressure powder X-ray diffraction was performed using diamond anvil cells (DACs) at the I15 beamline, at Diamond Light Source, UK. The X-ray energy was 29.2 keV (λ = 0.4246 Å) and a 2D CdTe Pilatus 2M area detector was used for data collection. Integration of 2D diffraction images was performed using the Dawn software,²⁹ while Rietveld refinements were performed using TOPAS-Academic V7 software package.³⁰ Silicone oil was selected as the pressure-transmitting medium, which can be expected to maintain hydrostatic conditions during compression within the measured pressure range.³¹ In this way, the isotropic application of pressure in the whole area of the sample can be achieved.³² The gasket material was 200 µm foil of steel, preindented to a thickness of 80-100 µm and with a 400 µm diameter hole EDM 'drilled' into it to form the sample chamber. Samples, ruby and silicone oil were loaded into the DAC under Ar inert atmosphere. Loaded samples were freely floating in the pressure medium and not bridging the anvils. The applied pressure was in a range from ambient to 1.5 GPa in Δp = 0.1 GPa steps. The pressure was adjusted using a LeToullec style membrane-type DAC with 700-micron culets and the pressure was determined by the Ruby luminescence method (see Supporting Information, Figure S1).^{33,34} An illustrative diagram including the ex-situ and in-situ application of pressure is now presented in the Supporting Information (Figure S1a and b).

High-pressure experiment. A Walker-type multi anvil high-pressure setup (1000t down force press (mavopress LPR1000-400/50) was used to apply a quasi-hydrostatic

pressure of 10 GPa to the Li₆PS₅Br powder. 20 mg of Li₆PS₅Br was loaded into a platinum capsule (99.95%, Ögussa, Vienna, Austria), to additionally prevent the material from exposure to air. The platinum capsule was placed into an α -BN (Henze Boron Nitride Products AG, Lauben, Germany) crucible, which has an inner diameter of 2.8 mm and an inner height of 5 mm. The crucible was closed with a lid of α -BN and placed in an MgO octahedron. All the handling and preparation of the octahedron was performed in an Ar glovebox. Completion of an 18/11-assembly with eight tungsten carbide cubes (Hawedia, Marklkofen, Germany) and loading in the press was carried out under air. More information about the high-pressure apparatus can be found in literature. 35-37 The pressure was increased to 10 GPa within 271 minutes and held for 60 minutes. The choice of 60 minutes was made after taking into consideration that the time does not influence the amount of induced strain in this material (See Supporting Information, Figure S2). Afterwards, the pressure was released to ambient conditions within 813 minutes. The octahedron was cracked in the glove box, and the crystalline sample was recovered from the surrounding parts with a spike. Each application of high-pressure loading yields an approximate total of 20 mg of Li₆PS₅Br powder, due to the small capacity of the α -BN crucible. Consequently, the 10 GPa sample is not included in all measurements within this study owing to limitations in mass availability.

Williamson-Hall analysis. According to the Williamson-Hall method, diffraction line broadening can be attributed to the presence of internal strain and grain size contributions, which have different functional dependencies on scattering angle, i.e., 2θ . The degree of peak broadening, quantified by the full width at half maximum (FWHM) or, more generally, the integral breadth (β) of the diffraction peaks, which can be extracted from X-ray diffraction data and used in the Williamson-Hall equation,

$$\beta \cos(\theta) = (C \varepsilon_{\text{XRD}}) \sin(\theta) + \frac{\lambda}{d_{\text{XRD}}}.$$
 (1)

This predicts a linear dependence of the quantity $\beta\cos(\theta)$ when plotted vs. $\sin(\theta)$ with the slope being a metric of the internal strain $\varepsilon_{\rm WH}=C\varepsilon_{\rm XRD}$, where C is a proportionality factor of the internal strain $\varepsilon_{\rm XRD}$ and the y-intercept can be related to the grain size, $d_{\rm XRD}$, and the wavelength, λ , of the X-rays.

To determine the integral breadth β , a pseudo-Voigt function is used to fit the intensity I of the diffraction peaks. Explicitly, each individual Bragg reflection was fit using the pseudo-Voigt function:

$$I(2\theta) = I_{max} [\eta L(2\theta - 2\theta_0) + (1 - \eta)G(2\theta - 2\theta_0)]. \tag{2}$$

This function is selected to fit the peaks, because of the split asymmetry of the peak broadening that can be present and it is the convolution of a Lorentzian, L and a Gaussian, G distribution function, where the Gaussian function, with weighting coefficient η . The prefactor I_{max} scales the maximum peak height for each Bragg reflection.

The Gaussian function has an exponential $2\theta-2\theta_0$ dependency, which is divided by the Gaussian peak width of the XRD reflections.

$$G(2\theta - 2\theta_0) = \exp\left(-\frac{\pi (2\theta - 2\theta_0)^2}{\sigma_G^2}\right). \tag{3}$$

The split-Lorentzian full width half maximum (Γ) was allowed to be different on the left and right side of the peak maximum and the split-Lorentzian function is given by:

$$L(2\theta - 2\theta_0) = \frac{(\Gamma/2)}{(2\theta - 2\theta_0)^2 + (\Gamma/2)^2}, \text{ with } \Gamma = \Gamma_L, 2\theta \le \theta_0 \\ \Gamma = \Gamma_R, 2\theta > \theta_0$$
 (4)

By fitting each diffraction peak according to Eqs. 2 – 4, and taking into consideration the baseline of each reflection, the integral breadth β was determined according to:

$$\beta = \frac{1}{I_{\text{max}} - I_{\text{baseline}}} \int_{2\theta_{min}}^{2\theta_{max}} I(2\theta) \, d2\theta \tag{5}$$

Where $2\theta_{min}$ and $2\theta_{max}$ define the range of each fitted diffraction peak, which is divided by the subtraction of the maximum value of intensity minus the corresponding value of the intensity from the baseline.

The Williamson-Hall approach does not specify the origin of the strain; isotropic or anisotropic and can therefore be applied regardless of the microscopic origin of the internal strain. The equations used to extract the value of the value of the dislocation density are also based on a modified Williamson-Hall method. The dislocation density $\rho_{\rm d}$ is defined as the total length of dislocation line per unit volume of crystal and is given by the following equation: ¹⁶

$$\Delta K = \frac{0.9}{d} + \left(\frac{\pi A^2 B_{\rm D}^2 \rho_{\rm d} C}{2}\right)^{1/2} K,\tag{6}$$

where, ΔK and K, in this modified Williamson-Hall equation equal to $\Delta K = (\Delta 2\theta)\cos\theta_{\rm B}/\lambda$ and $K = 2\sin\theta_{\rm B}/\lambda$, respectively. The wavelength of the CuKa is $\lambda = 1.5406$ Å. The full width at half maximum (FWHM) or integral breadth (β) of the corresponding diffraction peak at $\theta_{\rm B}$, is denoted by $\Delta 2\theta$, while $\theta_{\rm B}$ is the diffraction angle at an exact Bragg position. The parameter A is determined by the effective outer cut-off radius of dislocations (A=2), $B_{\rm D}$ is the Burger's vector and the constant C is an average dislocation contrast factor and can vary from 1 to 4, depending on the nature of the material.³⁹

$$\Rightarrow \Delta K = \text{slope } KC^{1/2} + \text{intercept},$$

$$(\pi A^2 B_{\rm D}^2/2) \rho_{\rm d}^{1/2} = slope \Rightarrow \rho_{\rm d} = \left[\frac{slope}{(\pi A^2 B_{\rm D}^2/2)^{1/2}}\right]^2$$
 (7)

Therefore, the dislocation density can be calculated, when knowing the slope of the $K-\Delta K$ graph.

Rietveld analysis and Stephens' anisotropic microstrain model analysis. Rietveld refinements were carried out using the TOPAS-Academic V7 software package.³⁰ An instrumental parameter file was created by refining a (001) Si standard for Cu-XRD data and a LaB₆ standard for the synchrotron data. The peak shape was modeled using a modified Thomson-Cox-Hastings pseudo-Voigt function which was refined to the peak shape of the LaB₆ standard for synchrotron data and the silicon standard for the Cu K α 1 XRD data. For the subsequent refinements, U, X, and Y were constrained to instrument values and W refined freely.⁴⁰ Fit indicators (e.g., R_{wp} and R_{exp}) were used to assess the quality of the refined structural models. The following parameters were initially refined: (1) scale factor, (2) background coefficients using a Chebyshev function with 10 free parameters, (3) zero-shift error, (4) peak shape, which was modeled using a modified Thomson-Cox-Hastings pseudo-Voigt function, (5) lattice parameters, (6) fractional atomic coordinates, (7) isotropic atomic displacement parameters, (8) atomic occupancies of the anions were then allowed to refine subsequently all other

parameters, to quantify the anion site disorder.⁸ In the final step, Stephens' anisotropic strain model was used to describe the internal strain, since significant anisotropic peak broadening was observed in the strained samples. The model allows for two independent strain parameters in a cubic system, S_{400} and S_{220} . When 'cubic equality' $S_{400} = 2S_{220}$ is not observed, the strain in the respective material can be considered to be anisotropic.⁴¹

High-pressure neutron powder diffraction. Neutron powder diffraction (NPD) under pressure (in-situ) was performed at the beamline BL-3, using the Spallation Neutrons and Pressure Diffractometer (SNAP), at the Spallation Neutron Source (SNS), at Oak Ridge National Laboratory (ORNL). NPD measurements under pressure were performed using a Paris-Edinburgh (P-E) press fitted with single-toroidal cubic boron nitride anvils^{42,43} from ambient pressure to 1.5 GPa, with an increasing step of 0.05 GPa. Pb was used as a pressure calibrant, since its reflections do not overlap with the reflections of Li₆PS₅Br. Samples were handled under He atmosphere and loaded into a null-scattering Ti-Zr alloy⁴⁴ encapsulated gasket. To ensure the safe transfer of the gasket out of the glovebox, the gasket was sealed via pressing at 0.05 GPa. Then, it was transferred into the P-E cell and the measurements were performed under room temperature (298 K). The data collection time was 6 h for each pressure (0.5 GPa, 1.0 GPa and 1.5 GPa). Data reduction was carried out using the Mantid software package.⁴⁵

Pair distribution function analysis. Total scattering data was collected using a Stoe STADI P diffractometer (Ag K $_{\alpha 1}$ radiation: λ = 0.55941 Å, Ge 111 monochromator) in Debye-Scherrer geometry with four Dectris MYTHEN2 1K detectors. The samples were measured in sealed borosilicate glass capillaries (Hilgenberg) with a diameter of 0.5 mm over a Q-range of 0.8-80 Å $^{-1}$. Data reduction was carried out using PDFgetX3 46 with a Q-range cutoff of Q_{max} = 12 Å $^{-1}$. Small box modeling was performed using TOPAS-Academic V7 software package. 30 The data were fitted over an r-range of 2-20 Å where (1) scale factor, (2) correlated motion factor, (3) lattice parameters, (4) atomic positions, and (5) isotropic atomic displacement parameters were subsequently refined.

Raman spectroscopy. Raman measurements were performed on Bruker SENTERRA II spectrometer which operates with a 532 nm laser and is equipped with an objective lens with 20-fold magnification. For every sample, three different spots were measured, by applying a laser power of 2.5 mW, an integration time of 1000 s and four co-additional measurements. The sample preparation was carried out in an Ar glovebox with $O_2 < 0.5$ ppm and $H_2O < 0.5$ ppm. Each powder sample was placed onto one microscope slide, framed with silicone vacuum grease and sealed air-tight with a microscope glass cover, to prevent the exposure of the samples to air and moisture during the measurement.

Nuclear magnetic resonance spectroscopy. Solid-state ³¹P magic-angle spinning (MAS) nuclear magnetic resonance (NMR) spectra were recorded on a Bruker DSX 500 spectrometer (11.74 T wide bore magnet with a Larmor frequency of 202.4 MHz), utilizing a 2.5 mm Bruker MAS probe. All experiments were conducted using a pulse length of 2.5 μ s, corresponding to a flip angle of $\pi/2$ at a nutation frequency of 100 kHz, and recycles delay of 100 s were used for the single-pulse excitation scheme. The samples were packed into 2.5 mm ZrO₂ rotors under Ar atmosphere (H₂O < 0.5 ppm and O₂ < 0.5 ppm). MAS was conducted at a spinning frequency of 25.0 kHz and the magic angle was calibrated using the ²³Na resonance of solid NaNO₃ under MAS. The ³¹P chemical shift scale was referenced to phosphoric acid (H₃PO₄, 85 %) at 0 ppm. Static saturation-recovery ⁷Li NMR experiments were conducted at different temperatures to determine T_1 on a Bruker Avance III 300 spectrometer equipped with a wide bore magnet which operates at 300 MHz (7.05 T) using a broadband NMR probe (Bruker, VTN). Samples were packed into 4 mm MAS rotors in an Ar glovebox (H₂O < 0.1 ppm and $O_2 < 0.1$ ppm). All experiments were conducted at a resonance frequency of 116.6 MHz with a pulse length of 2.5 µs corresponding to a nutation frequency of 100 kHz. The length of the recovery delay was increased in four steps per decade from $t_1 = 10^{-5}$ s to $t_{28} = 56.234$ s. The Fourier transformed signals were integrated in TopSpin and the resulting signal intensity curves were fitted using an exponential saturation function with stretching exponent.⁴⁷ The temperature of the sample was regulated by using a nitrogen gas flow and electrical heating. Cooling of the nitrogen gas in the temperature range from 200 K to 290 K was achieved with an Air Jet XR compressorbased cooling system from SP Scientific (FTS Systems). An uncooled nitrogen gas flow was used to control the temperature in the range from 320 K to 440 K. ¹H NMR spectra of methanol (200 K to 290 K) and ethylene glycol (320 K to 440 K) were recorded to externally calibrate the temperature with the occurring shifts in signal frequency.⁴⁸

Impedance spectroscopy. AC impedance spectroscopy was conducted on freestanding pellets made from powders of the materials pressed at various pressures (0.5 GPa, 1.0 GPa, 1.5 GPa and 10.0 GPa). After the materials were subjected to their respective pressures, the resulting pellets were hand ground and approximately 220 mg of the powders were hand pressed into pellets again to ensure comparable pellet densities. All pellets were pressed isostatically at 410 MPa for 45 minutes, resulting in experimental densities of approximately 88%. Then, gold electrodes were sputtered onto the pellets. The pellets were then contacted with aluminum current collectors and fixed into pouch cells. The impedance spectra were recorded using an Alpha-A impedance analyzer (Novocontrol Technologies) in a temperature range from 298 K to 173 K (one hour of equilibration time per temperature step), utilizing an AC excitation voltage of 10 mV in a frequency range of 5 MHz to 100 mHz. Due to the much smaller sample volume available from the high-pressure 10 GPa sample, a press cell with smaller diameter was used for the calculation of the ionic conductivity and the SP-300 analyzer which can probe a smaller temperature range. The RelaxIS 3 software (rhd instruments) was utilized for data evaluation and data quality was tested using the frequency range for fitting of the data using the Kramers-Kronig analysis. Uncertainties of the ionic conductivity were calculated from the standard deviation of the triplicate measurements.

Solid-state battery assembly and evaluation of the strained $\text{Li}_6\text{PS}_5\text{Br}$ as catholyte. To investigate the influence of the strain in the structure of $\text{Li}_6\text{PS}_5\text{Br}$ on the battery performance, solid-state battery half cells were assembled. The preparation of the cell building was carried out in a glovebox under Ar atmosphere ($\text{H}_2\text{O} < 0.5 \text{ ppm}$ and $\text{O}_2 < 0.5 \text{ ppm}$). Commercial $\text{LiNi}_{0.83}\text{Co}_{0.11}\text{Mn}_{0.06}\text{O}_2$ (NCM-83, MSE supplies) was dried overnight at 250°C, under vacuum, in a Büchi B-585 glass oven prior to use. For the composite cathode, the $\text{Li}_6\text{PS}_5\text{Br}$ -pressed at 0.5 GPa and $\text{Li}_6\text{PS}_5\text{Br}$ -pressed at 1.5 GPa were used as catholyte and NCM-83 was used as the cathode active material in a mass

ratio of 65:35 (NCM-83: Li_6PS_5Br), with the configuration of $In/LiIn|Li_6PS_5Br|NCM-83:Li_6PS_5Br$.

The materials were put in a 5 mL ball mill cup with three 5 mm diameter ZrO_2 balls. The cup was sealed with parafilm to prevent the exposure of the composite to air and moisture and was soft milled at 15 Hz for 15 minutes. For the cell assembly, 80 mg of Li₆PS₅Br (unstrained) was used as the separator, filled in the press cell and tightened by hand. After hand-pressing, 12 mg of the composite cathode was distributed homogeneously onto the surface of the separator. Subsequently, 3 tons of pressure (380 MPa) was applied uniaxially for 3 minutes. Then, lithium foil was cut from a lithium rod (abcr, 99.8%) with a mass between 1.5 mg and 1.8 mg and indium foil (chemPUR, 100 µm thickness, 9 mm diameter, 99.999%) was used as the anode to ensure a stable alloy during cycling. The freshly prepared lithium foil and indium foil were used to form the In/LiIn anode in-situ. The press cell was fixed in an Al frame and tightened by applying force of 10 Nm with a torque, resulting in 50 MPa of stack pressure. Triplicates were built for each composite, to ensure the reproducibility of the results. For short-term cycling, the cells were charged to 3.7 V vs. In/LiIn and discharged to 2.0 V vs. In/LiIn at 25 °C, by applying a current density of $j = 0.165 \text{ mA} \cdot \text{cm}^{-2}$ corresponding to a rate of 0.1 C. The PEIS measurements were performed at T = 298 K using a BioLogic VMP-300 potentiostat. An AC excitation voltage of 10 mV was applied, and impedance spectra were recorded in a frequency range of 7 MHz to 10 mHz. For further evaluation of the data, including the fitting of the Nyquist plots and transmission line modelling (TLM) analysis the RelaxIS 3 software (rhd instruments) was used. The data quality was assessed by Kramers-Kronig analysis to determine the reliable frequency range for fitting of impedance data.

Partial charge transport measurements. For the partial ionic transport measurements, 100 mg of composite with a weight ratio of 65:35 (NCM-83: Li₆PS₅Br) were used. The mixture was transferred into a 15 mL ZrO₂ cup with 5 mm sized ZrO₂ balls and mixed using a frequency ball mill (Fritsch pulverisette 23 Mini Mill) at a frequency of 15 Hz for 15 minutes. As electronically blocking electrodes, 80 mg of Li_{5.5}PS_{4.5}Cl_{1.5} were placed on each side of the composite. The airtight cell was pressed uniaxially at 3 tons for 5 minutes and then indium foil (diameter 9 mm) and pressed

lithium (1.5 mg) was placed on both sides of the solid electrolyte. For the effective electronic transport measurements, 100 mg of composite was used, and steel stamps were used as ionic blocking electrodes on both sides. The cell was closed airtight and was pressed uniaxially at 3 tons for 3 minutes. The cells were placed in a metal frame to apply a pressure of 50 MPa and were left for 6 hours at 25 °C for equilibration.

Potentiostatic electrochemical impedance spectroscopy (PEIS) was performed at 298 K, using a Biologic VMP 300 potentiostat for the determination of the ionic conductivity of the symmetric cell with ionic blocking electrodes. An excitation amplitude of 10 mV and a frequency range from 10 mHz to 7 MHz were used. Following the impedance measurement, a subsequent DC polarization measurement was performed. A voltage from -45 mV to 50 mV increased stepwise by 5 mV, while each voltage step was kept for 2 h for equilibrium. For the measurements of the effective ionic conductivity, the same conditions were used for the impedance spectroscopy. The DC polarization measurement was performed in a voltage range from 0.5 mV to 5 mV, with an increasing step of 0.5 mV. For the equilibrium, each voltage step was measured for 6 hours to ensure full polarization.

RESULTS AND DISCUSSION

Straining of the solid electrolyte. Two different approaches based on powder X-ray diffraction were used to analyze the structure of the argyrodite. In the first approach, the structures of the pristine material and the pressed materials were studied ex-situ, after releasing the applied pressure from the samples (Figure 2a, 2b). In addition, to gain deeper insight into the structural changes occurring in the Li₆PS₅Br during the applied pressure, in-situ diffraction was performed under hydrostatic conditions (Figure 2c, 2d). These two approaches allow the monitoring of structural changes in Li₆PS₅Br during and after pressure release. Looking at the ex-situ diffraction data, no evidence for a phase transition or amorphization process is visible for the argyrodite up to pressures of 1.5 GPa (Figure 2a). A significant broadening of the reflections reveals that internal strain has been induced in the structure, which remains present after the pressure release (Figure 2b). The in-situ measurements corroborate the reflection broadening in hydrostatic conditions (Figure 2c), meaning that the strain in the structure can be induced by either uniaxial or hydrostatic pressure. The in-situ measurements also confirm the retention of the Li₆PS₅Br argyrodite structure for pressures up to 1.5 GPa. As the applied pressure is increasing, the broadening of the reflections becomes more pronounced (Figure 2a, 2c). The difference between the exsitu and in-situ measurements can be seen, when comparing Figures 2b and 2d. After pressure release, only the reflection broadening is present in the samples. However, in the in-situ experiments, an additional shift additionally to higher Q, corresponding to an in-situ unit cell contraction (Supporting Information, Table S1).

To further investigate if the broadening can be increased further, the material was pressed at 10 GPa (Figure 2a). The X-ray diffraction pattern indicates that the material is not amorphized, but rather shows an even pronounced broadening of the reflections. The Rietveld refinements against the diffraction data can be found in the Supporting Information (Figure S3 and S4).

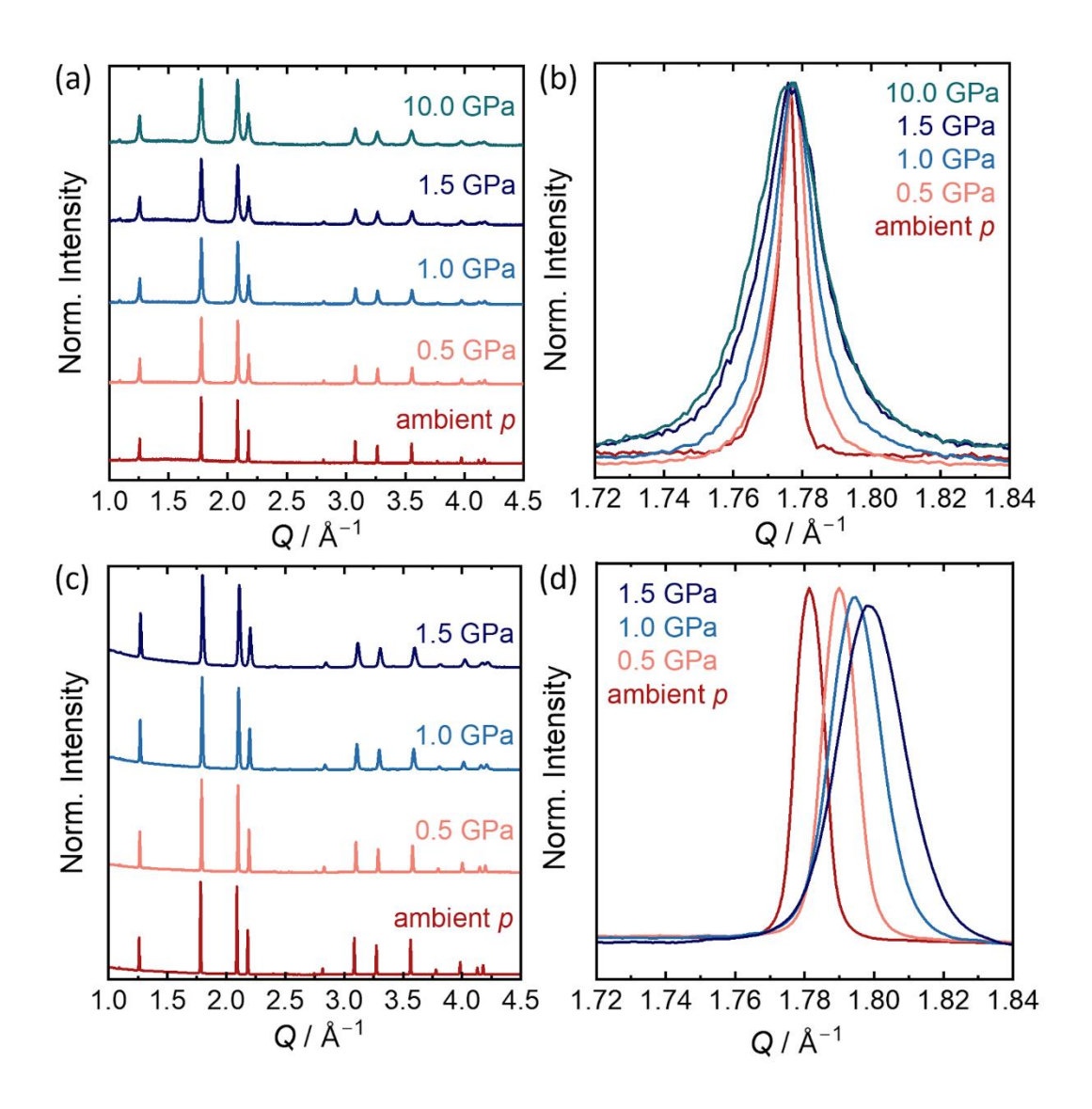


Figure 2. Strain induced by pressure revealed from ex-situ and in-situ X-ray diffraction. (a) and (b) The broadening of reflections as a function of increasing pressure in the ex-situ diffraction. (c) and (d) The increase of strain and the concomitant Q-shift as a function of increasing pressure revealed by the in-situ diffraction.

Quantitative and qualitative analysis of strain. Williamson-Hall analyses (Figure 3a) of the ex-situ X-ray diffraction measurements are used to quantify the internal strain ε_{WH} (%) of the samples as a function of applied pressure (Figure 3b). The good matching of the Williamson-Hall analyses of the in-situ and ex-situ measurements can be found in the Supporting Information, Figure S5. In addition, the anisotropic strain model by Stephens via Rietveld refinements are used to quantify the strain ε_{RR} from the in-situ diffraction data due to the higher data quality. The slope of the Williamson-Hall graph for the ex-situ data (Figure 3a) is $\varepsilon_{WH} = C\varepsilon$, where ε is the internal strain within the

material and the constant C has typical values between 0.5 and 4 depending on the material and nature of the internal strain. ⁴⁹ Thus, $\varepsilon_{\rm WH}$ is expected to be proportional to the actual internal strain in the material. Here, we consider C=1, to simplify the analysis. Figure 3b shows that with increasing pressure, more microstrain is found in the material. The relationship between the strain obtained from the Williamson-Hall analysis, $\varepsilon_{\rm WH}$ and from the Stephens' anisotropic strain model, $\varepsilon_{\rm RR}$ is shown to be linear (Figure 3c). Therefore, the choice of the constant C=1 is validated and confirms the accurate calculation of strain from both methods in these powdered materials. With higher pressure on the material, higher amounts of strain can be found.

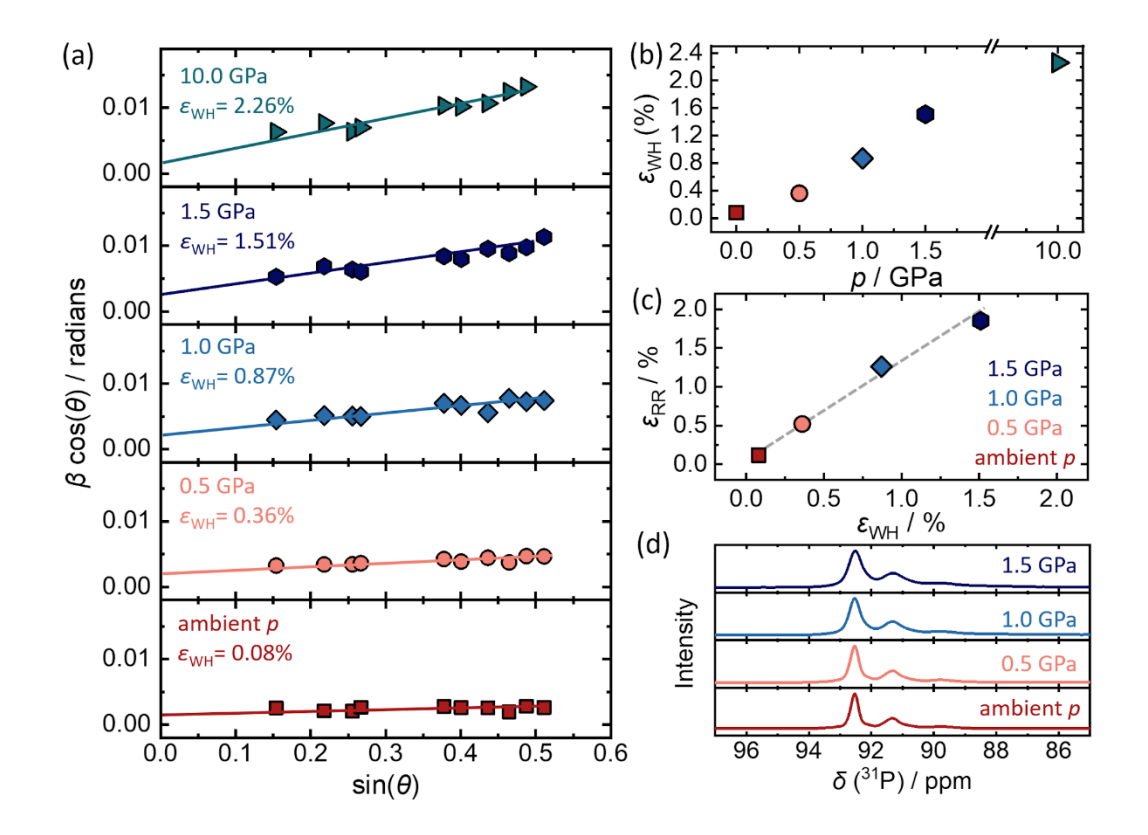


Figure 3. Williamson-Hall analysis of 10% Br^-/S^{2-} Li_6PS_3Br . (a) Williamson-Hall plots for all applied pressures. Increasing pressure results in increased internal strain of Li_6PS_5Br characterized by the slope ε_{WH} . (b) Internal strain vs. pressure in Li_6PS_5Br showing that with more pressure, more strain is induced. (c) The amount of internal strain determined from the Williamson-Hall method agrees well with that determined from Stephens' anisotropic strain model. (d) ^{31}P MAS NMR spectra reveal broadening of the resonances.

Structural effects of strain on the solid electrolyte. Typically, the site-disorder between the halide and sulfide anions in argyrodites has been shown to affect the

materials' properties. Here, the Rietveld refinement analyses also show that the degree of Br⁻/S²⁻ site disorder is not significantly impacted by the application of pressure up to 1.5 GPa (see Supporting Information, Table S1). To verify the structural understanding from the diffraction experiments, ³¹P NMR spectra were obtained for the unstrained and strained materials (Figure 3d). The ³¹P NMR spectra for untreated and treated Li₆PS₅Br show multiple resonances located at 92.5 ppm, 91.3 ppm, 89.8 ppm, 88 ppm, and 83 ppm. These can be assigned to combinations of the Br⁻/S²⁻ mixed site configurations of the second coordination sphere around the PS₄³⁻ units. The highest ³¹P shift can be assigned to a 4SOBr configuration, while the lowest shift can be assigned to 0S4Br mixing. The ³¹P NMR spectra after applying different pressures (Figure 3d) reveal a broadening of all resonances as the strain increases in the Li₆PS₅Br structure in accordance with the X-ray diffraction results. Therefore, the higher strain found in X-ray diffraction data is accompanied with a higher line broadening in ³¹P NMR spectra. In addition, ⁷⁹Br and ⁶Li and ³³S NMR spectra were collected (Figure S6), showing only minor changes for all the different applied pressures.

Origin of strain. It is important to understand the underlying mechanism causing the internal strain. The most plausible explanation is that applying pressure results in plastic deformation and the introduction of dislocations into the material. Dislocation densities can be estimated from the slope of the modified Williamson-Hall plot (Figure S7). Even though these estimated dislocations densities require several assumptions about the nature of the dislocations (for procedure see Experimental Section), it is expected to give qualitative insights,³⁸ revealing that a higher dislocation density corresponds to more internal strain (Figure 4a).⁵¹ Along with X-ray diffraction, dislocation densities can be measured through neutron diffraction (indirect method) and transmission electron microscopy (direct method).⁵² Neutron diffraction under pressure was performed to explain the nature of the dislocations and the results can be found in the Supporting Information (Figure S8). Despite the high neutron flux, the small amount of material in the in-situ neutron cell during the measurement (~30 mg) was not sufficient to obtain a reasonable signal-to-noise-ratio in the data sets, so further analysis of the neutron diffraction measurements is prevented. However, as visible in Figure S8, significant reflection broadening with increasing pressure is observed in the neutron diffraction data. The comparison of dislocation densities using all available methods would be helpful, however the argyrodites are unstable under the high electron doses in transmission electron microscopy, making this analysis unfeasible for the purpose of this study.

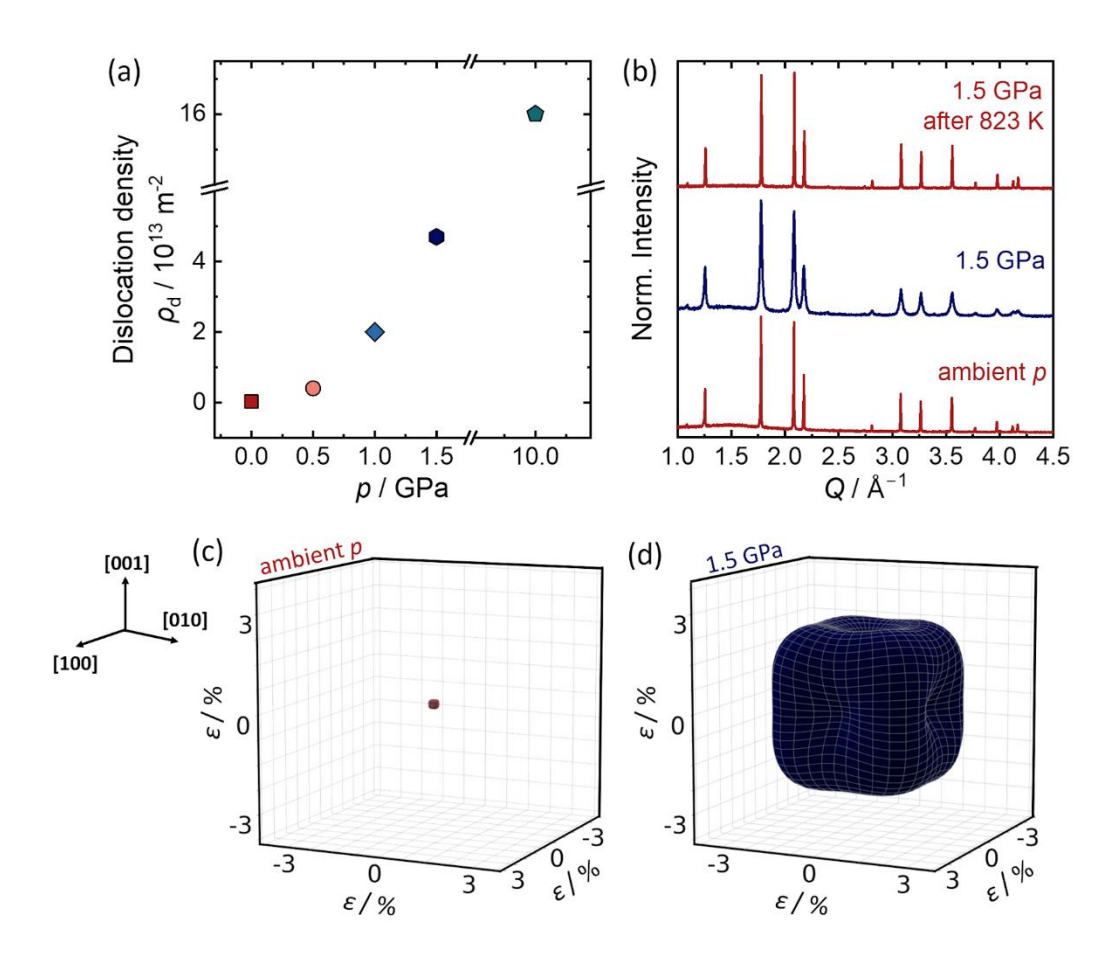


Figure 4. Strain in the form of dislocations in the structure. (a) The dislocation densities calculated from the Williamson-Hall analyses. (b) Annealing of the material results in its return to the original structure, suggesting dislocations are a likely source of the internal strain. (c, d) The strain contour plots for the (c) unstrained and (d) strained material after 1.5 GPa, as obtained from the generalized strain model, showing anisotropic strain distribution in the argyrodite structure.

X-ray diffraction analysis shows that the strained material, upon being subjected to annealing at 823 K, returns to its original state (Figure 4b). This temperature was selected because it aligns with the synthesis temperature of Li₆PS₅Br. During annealing, the dislocation density decreases; equals to the initial value of the unstrained material, leading to the relaxation of strain in the material. This observation corroborates a

dislocation mechanism, as dislocations are known to anneal out with temperature.⁵³ The decrease in dislocation densities can be attributed to two key mechanisms: dislocation annihilation involving dislocations possessing same Burger's vectors, and dislocation absorption involving dislocation with different Burgers vectors, occurring at grain boundaries. 53 More specifically, dislocation absorption at grain boundaries occurs as dislocations migrate and interact with the boundaries between individual grains in the material. During this process, dislocations can be absorbed or incorporated into the grain boundaries, further reducing the overall dislocation density and promoting strain relaxation. The observed restoration of the original structure through dislocation annealing provides insights into the material's response to thermal treatments and its ability to recover from deformation-induced strain. Anisotropic strain refinement reveals the predominant orientation of the strain in the structure in the S220 vector direction. 40 The distinction between the unstrained material and the material after 1.5 GPa can be visualized by the strain contour plot (Figure 4c, 4d), which shows how the strain distribution varies in a three-dimensional region. The plots were created using obtained Stephens' strain values from the Rietveld refinements. 40,41 The contour plots for all applied pressures can be found in the Supporting Information, Figure S9.

Influence on the local structure. Pair distribution function analyses (Figure 5) and Raman spectroscopy (Figure S10) were performed to investigate differences in the short-range order of the argyrodites. The introduction of more dislocations, when the material is pressed up to 10 GPa, should lead to a local change in the arrangement of atoms in the argyrodite structure. However, no significant differences in the G(r) are observed up to 20 Å and the distribution of distances among the atoms seems to be unaffected. The refinement results of the G(r) can be found in the Supporting Information, Figure S11. Nevertheless, considering that dislocations perturb the coherence length, a closer look at the longer r-range in the pair distribution functions (Figure 5b) shows a faster loss of G(r) the higher the applied pressure was. By using the spherical diameter approach to fit the data a much lower coherence can be found, corresponding to 14 nm in the material pressed at 10 GPa, compared to 46 nm in the unpressed sample.

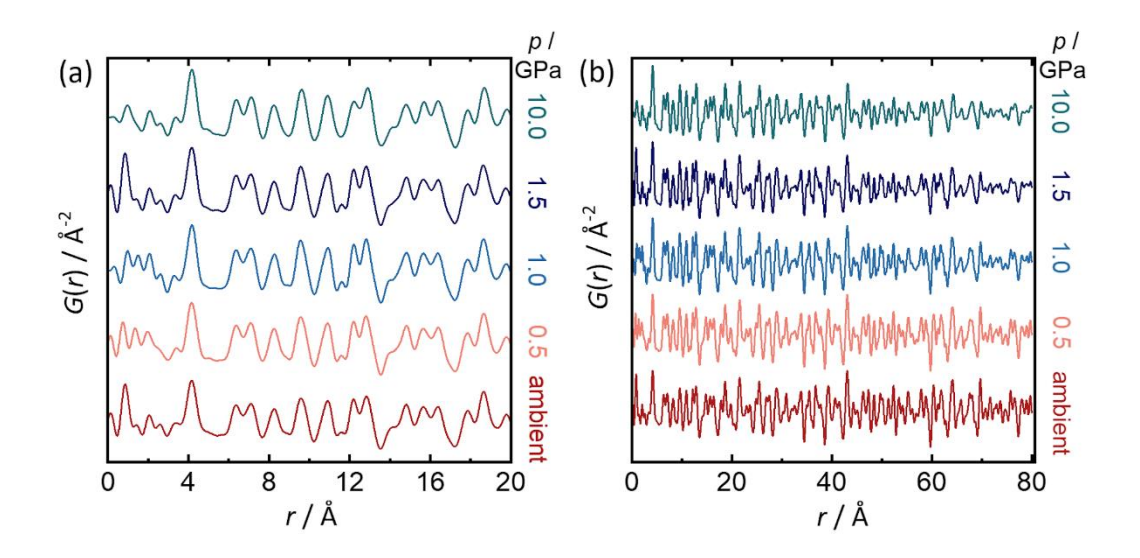


Figure 5. Pair distribution function analysis shows the effect of strain in the local structure in Li_6PS_5Br . (a) PDF shows no significant difference in the argyrodite structure between the unstrained and strained materials in the short-range. The difference curve of the fit is depicted by the blue lines. (b) A significant decrease of the coherence length is observed with higher strain.

Influence on the ionic transport. The influence of the strain on the ionic conductivities and the activation energies of Li₆PS₅Br is probed by temperature dependent electrochemical impedance spectroscopy. Low-temperature impedance data was acquired from 173 K to 298 K for all samples up to 1.5 GPa. Due to the much smaller sample volume available from the high-pressure 10 GPa sample, a smaller temperature range had to be probed. The impedance data was fit with an equivalent circuit model. This model consists of a parallel connection of a resistor and a constant phase element (CPE), both in series to a second CPE. The first CPE corresponds to the internal capacitance of the argyrodite powder, and the second CPE corresponds to the electrode blocking behavior (Figure 6a). The temperature dependent ionic conductivities exhibit linear Arrhenius behavior (Figure 6a) and reveal that the activation energies associated with Li⁺ jumps in both strained and unstrained Li₆PS₅Br remain unchanged (within uncertainty), however a shift to higher ionic conductivities can be seen. Here, an increase in internal strain seems to correspond to an increase in ionic conductivity (Fig. 7a). To ensure reproducibility of the results, triplicate measurements were performed on three separately pressed samples. The activation energy extracted from the Arrhenius plots equals to $E_A = 0.36 \pm 0.01$ eV (Figure 6b). Although triplicate measurements of three separately pressed samples were not possible for the sample pressed at 10 GPa, due to the limited sample mass, the results fit into the general trend. The induced strain in the structure does not appear to affect the energy barrier for long-range Li⁺ jumps within Li₆PS₅Br. This finding suggests that the structural changes induced by pressure do not significantly influence the energy barrier for Li⁺ jumps. The material at ambient pressure is not included in the analysis, because the pellet preparation includes the isostatically pressing at 410 MPa prior to the impedance measurements (see Experimental Part) and therefore already induces internal strain in Li₆PS₅Br (see Supporting Information, Figure S12).

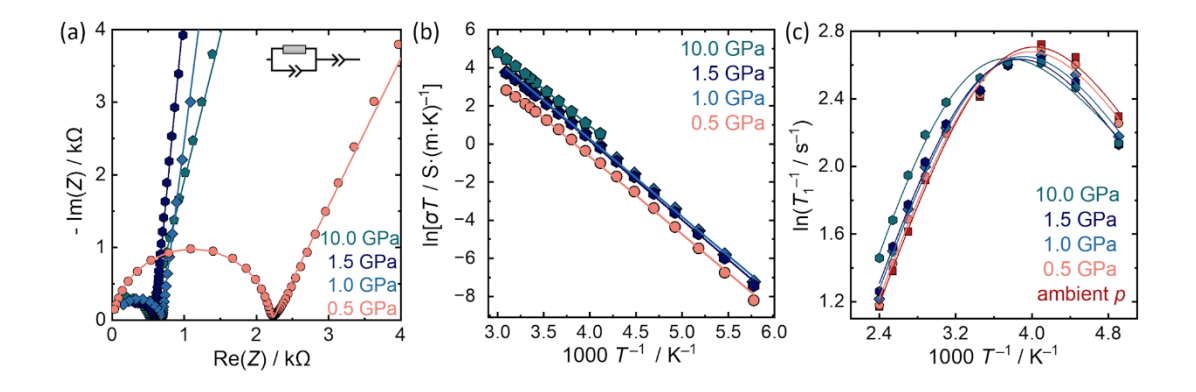


Figure 6. Determination of E_A and σ_{ion} from temperature-dependent impedance spectroscopy. a) Representative Nyquist plots of the strained materials acquired at room temperature. The various shapes represent the experimental data and the lines show the fit. b) Arrhenius plots of Li₆PS₅Br reveal that activation energies are consistent (within uncertainty) in the strained materials. (b) T_1 relaxation above and below room temperature, which verified the consistency of the activation energies for all materials (within uncertainty). A shift in the peak to higher temperatures is indicative of slower ionic transport.

The ionic conductivity shows more than two-fold increase in the higher strained materials compared to the least strained one. This finding suggests that strain engineering can be used to improve the ionic conductivity in solid electrolytes. Impedance spectroscopy is utilized to capture the long-distance transport of Li⁺ within the material, providing a comprehensive understanding of bulk Li⁺ motion. In contrast, ⁷Li NMR spectroscopy can distinguish Li⁺ jump processes in the bulk material at shorter time scales. In this study, ⁷Li NMR spectroscopy is employed to further investigate the

changes in activation energies in strained Li₆PS₅Br, compared to the findings obtained from impedance spectroscopy. The Arrhenius plot of the spin-lattice relaxation times T_1 obtained from ⁷Li relaxometry (Figure 6c) confirms that the activation energies are unchanged within statistical error. The activation energies and the pre-exponential time constants or residence time (τ_0) were obtained from fitting the relaxation rate curves with a modified BPP model.⁴⁷ Although the magnitude of E_A is different from that determined from the impedance measurement, which has been observed before in argyrodite solid electrolytes,⁵ the trend is the same. Spin-lattice relaxometry can be used to estimate the correlation time τ of the mobile ions between hopping events, at a given temperature T (see Table S2 for exact values). Fitting the BPP model to the data below room temperature (Figure 6c), we find that the more strained materials have progressively larger residence times. This can be observed directly from the maximum of the data (Figure 6c) shifting to higher temperatures, indicating slower transport for higher pressures. Using the relation $\tau = \tau_0 e^{E_{\rm A}/kT}$, we find that the correlation time τ is higher for higher pressures. It is important to note that this is the opposite trend as is observed from impedance spectroscopy (Figure 7a). At this stage, one may assume that the dislocations indeed negatively affect the local jump process. However, it may just be possible that the Li⁺ can diffuse faster, by using the existing dislocation cores as pathways, similar to pipe diffusion. 17,18 This would be in line with an unchanged activation barrier, suggesting a higher pre-factor and potential change in diffusion pathway or mechanism. Overall, the long-range transport is improved by a factor of about 2 (within triplicate measurements), further motivating investigations of transport in defective ionic conductors, especially as a function of internal strain and dislocation density.

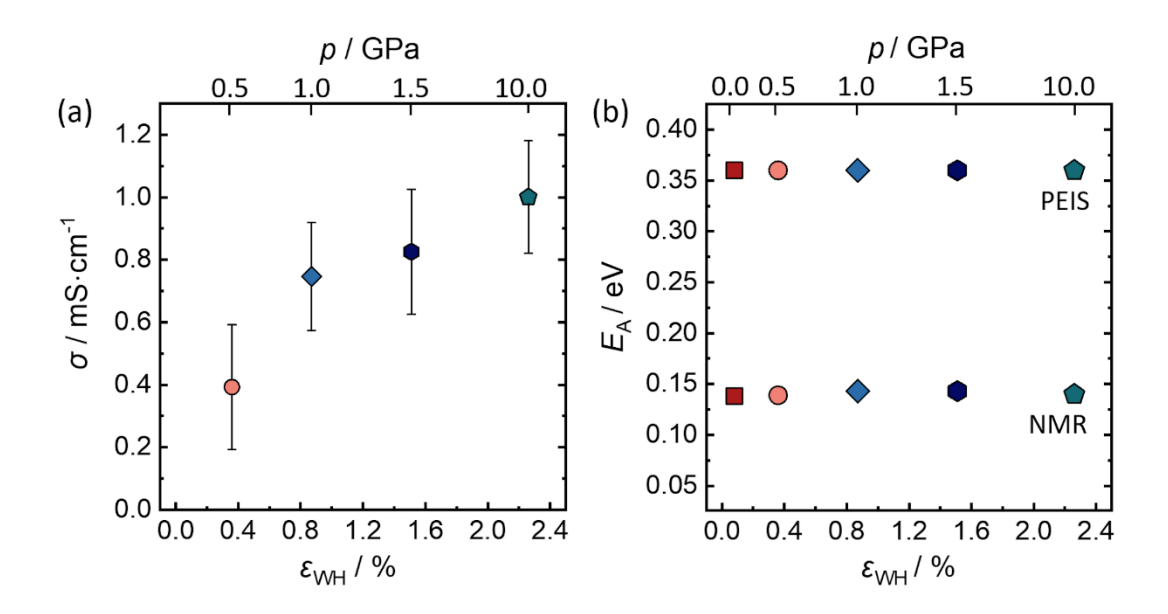


Figure 7. How transport is affected in local vs in long range. (a) A twofold increase in the ionic conductivity within triplicate measurements is observed, probed by impedance spectroscopy. (b) The activation energies show no difference with higher strain values, as calculated from NMR and impedance spectroscopy.

Half-cell testing with strained Li₆PS₅Br and charge transport measurements. The increased ionic conductivity of the strained Li₆PS₅Br opens the question if higher ionic conductivity or strain in the structure result in a higher performance of solid-state batteries incorporating the strained solid electrolytes. Besides comparing the performance of strained and unstrained Li₆PS₅Br as catholytes (solid electrolyte in the composite cathode) in solid-state batteries, an analysis of the partial transport properties is important. A balance of partial ionic transport is required in composite cathodes to achieve high utilization of the theoretical capacity of the active material during cell cycling.^{54,55} First, the different strained materials were tested as catholytes in solid-state batteries using LiNi_{0.83}Co_{0.11}Mn_{0.06}O₂ (NCM-83) as the cathode active material. For the construction of the In/LiIn | Li₆PS₅Br | NCM-83:Li₆PS₅Br (strained) solid state-batteries we chose the materials pressed at 0.5 GPa and 1.5 GPa as catholyte in the composite cathode. A comparison to an unstrained material is not useful, as the applied pressure during cell construction already amounts to 0.4 GPa (see Experimental Part). Cell testing with the samples pressed at 10 GPa was not possible due to the limited amount of sample and so the "highest" and "lowest" reasonably strained samples were used. A stable charge capacity of $160 \text{ mAh} \cdot \text{g}_{\text{CAM}}^{-1}$ can be

achieved for both catholytes within the first thirty cycles. The difference in the initial value of the charge capacity is normally observed in solid-state batteries and results from irreversible structural rearrangement, loss of available lithium, and chemomechanical effects. Overall, based on the capacities, the cells show similar performance and no significant influence on the long-term cycling stability can be found. This is expected as the long-term cell performance is strongly determined by ongoing interfacial decompositions.

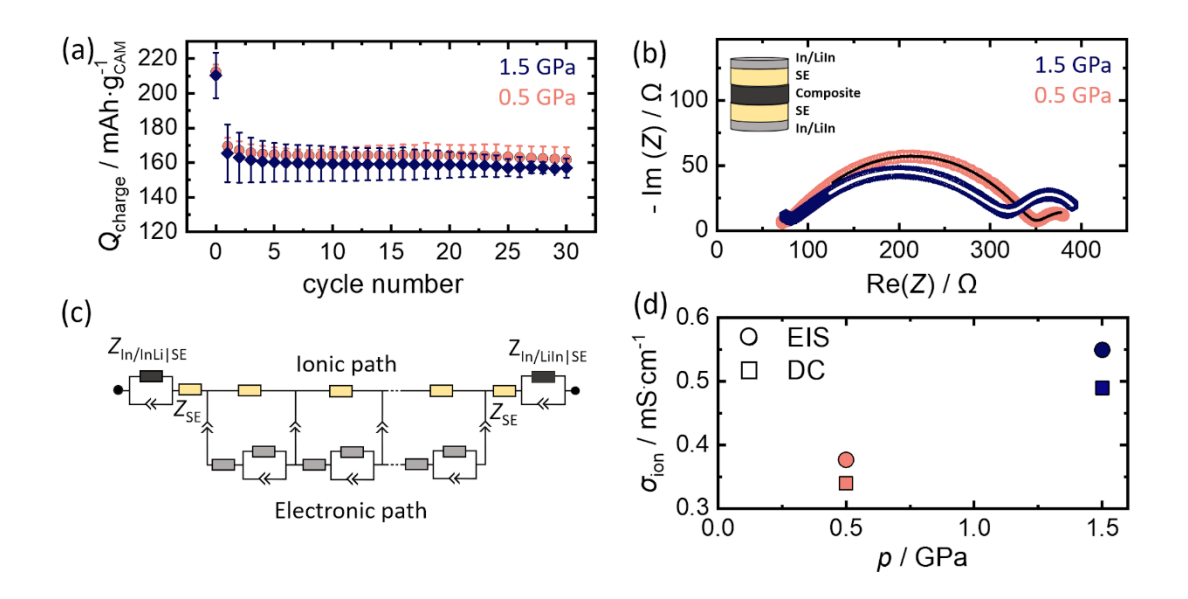


Figure 8. How strain impacts the performance of Li_6PS_5Br in cycling. (a) Similar solid state battery performance of Li_6PS_5Br pressed at 0.5 GPa and 1.5 GPa. (b) Nyquist plots show that the ionic conductivity of the most strained material in the composite is higher. (c) Schematic representation of the transmission line model used to fit the impedance data during cycling. (d) Comparison of the values of ionic conductivity obtain by impedance and DC polarization measurements.

To further evaluate the unstrained and strained Li₆PS₅Br behavior in the cathode composite, transmission line modelling of the impedance spectra and DC polarization was used in an electronic blocking system (Figure 8c). More detailed information on the approach can be found elsewhere.^{55,59} The strained material reveals higher effective ionic conductivity in the composite compared to the unstrained material (Figure 8b). This finding indicates that the strain that favors the ionic conductivity in the bulk electrolyte also extends to the electrode composite. Nevertheless, the minor improvement in the partial ionic transport does not seem to significantly affect the

solid-state battery performance. Considering that solid-state batteries are compressed under higher pressures — which will clearly induce strain in the argyrodite solid electrolyte — no significant direct influence of that strain on the battery performance is found here.

CONCLUSION

In this work, internal strain and dislocations are induced into the structure of Li₆PS₅Br by applying uniaxial and hydrostatic pressures. Using a combination of ex-situ powder X-ray diffraction and in-situ synchrotron high-pressure powder X-ray diffraction, we reveal that the increasing pressure results in increasing strain and dislocation densities. While pair distribution function analyses and Raman measurements reveal no change in the low-r range local structural arrangement, however a faster loss of G(r) is observed in the longer r-range, revealing the lower coherence in the more strained material. In addition, the increased internal strain is related to higher overall Li⁺ conductivity. This work shows that strain engineering can be used to increase the ionic conductivity in solid electrolytes without altering the composition. In addition, the pressures needed to induce strain in argyrodites lies in the range of typical solid-state battery fabrication. By testing the influence of strain in catholytes, to see how the twofold enhanced ionic conductivity impacts the material's performance in solid-state batteries, it is possible to show that the improved ionic transport of the bulk solid electrolyte extends into the partial ionic transport in the cathode composites. While faster transport in composites is necessary, fortunately, the overall performance of the solid-state batteries remain unaffected.

Overall, this work provides a first experimental report of how dislocation densities can be brought into Li⁺ conducting argyrodites via external pressure, opening up new routes for modulating ionic transport in the mechanically soft sulfide-based superionic conductors.

SUPPORTING INFORMATION

Graphical representation of the different pressure set-up; XRDs of the impact of time on strain; change in lattice parameters; Rietveld refinements for in-situ and ex-situ diffraction data; Williamson-Hall analysis for the in-situ data; Solid-state NMR ⁶Li, ⁷⁹Br and ³³S spectra, calculation of dislocation densities; neutron-diffraction measurements under pressure; strain contour plots; Raman spectra; PDF data; Williamson-Hall plot for the pellet pressed at hydrostatic conditions.

ACKNOWLEDGEMENTS

The research was supported by the Deutsche Forschungsgemeinschaft (DFG) under grant number ZE 1010/12-1. We further acknowledge funding from the Deutsche Forschungsgemeinschaft under project number 459785385. Stefan Schwarzmüller also acknowledges funding from the DFG within the Walter Benjamin Programme (SCHW 2168/1-1). This work used resources at the Spallation Neutron Source, a DOE Office of Science User Facility operated by the Oak Ridge National Laboratory and was carried out at BL-3, SNAP instrument (reference no. IPTS-29226.1). Some part of this research was carried out with the support of Diamond Light Source, instrument I15 (reference no. CY31791). The authors would also like to thank the beamline scientist Dr. Christopher A. Tulk for his assistance during the neutron measurements and the senior scientist Dr. Malcolm Guthrie for his assistance with reduction of neutron data.

REFERENCES

- (1) Manthiram, A.; Yu, X.; Wang, S. Lithium Battery Chemistries Enabled by Solid-State Electrolytes. *Nat. Rev. Mater.* **2017**, *2* (4), 1–16. https://doi.org/10.1038/natrevmats.2016.103.
- (2) Zhang, Z.; Shao, Y.; Lotsch, B.; Hu, Y.-S.; Li, H.; Janek, J.; Nazar, L. F.; Nan, C.-W.; Maier, J.; Armand, M.; Chen, L. New Horizons for Inorganic Solid State Ion Conductors. *Energy Environ. Sci.* 2018, 11 (8), 1945–1976. https://doi.org/10.1039/C8EE01053F.
- (3) Zheng, F.; Kotobuki, M.; Song, S.; Lai, M. O.; Lu, L. Review on Solid Electrolytes for All-Solid-State Lithium-Ion Batteries. *J. Power Sources* **2018**, *389* (February), 198–213. https://doi.org/10.1016/j.jpowsour.2018.04.022.

- (4) Kraft, M. A.; Ohno, S.; Zinkevich, T.; Koerver, R.; Culver, S. P.; Fuchs, T.; Senyshyn, A.; Indris, S.; Morgan, B. J.; Zeier, W. G. Inducing High Ionic Conductivity in the Lithium Superionic Argyrodites Li 6+ x P 1– x Ge x S 5 I for All-Solid-State Batteries. *J. Am. Chem. Soc.* **2018**, *140* (47), 16330–16339. https://doi.org/10.1021/jacs.8b10282.
- (5) Gautam, A.; Sadowski, M.; Ghidiu, M.; Minafra, N.; Senyshyn, A.; Albe, K.; Zeier, W. G. Engineering the Site-Disorder and Lithium Distribution in the Lithium Superionic Argyrodite Li 6 PS 5 Br. Adv. Energy Mater. 2021, 11 (5), 2003369. https://doi.org/10.1002/aenm.202003369.
- (6) Ohno, S.; Banik, A.; Dewald, G. F.; Kraft, M. A.; Krauskopf, T.; Minafra, N.; Till, P.; Weiss, M.; Zeier, W. G. Materials Design of Ionic Conductors for Solid State Batteries. *Prog. Energy* **2020**, *2* (2), 022001. https://doi.org/10.1088/2516-1083/ab73dd.
- (7) Till, P.; Agne, M. T.; Kraft, M. A.; Courty, M.; Famprikis, T.; Ghidiu, M.; Krauskopf, T.; Masquelier, C.; Zeier, W. G. Two-Dimensional Substitution Series Na 3 P 1– x Sb x S 4– y Se Y: Beyond Static Description of Structural Bottlenecks for Na + Transport. *Chem. Mater.* **2022**, *34* (5), 2410–2421. https://doi.org/10.1021/acs.chemmater.1c04445.
- (8) Kraft, M. A.; Culver, S. P.; Calderon, M.; Böcher, F.; Krauskopf, T.; Senyshyn, A.; Dietrich, C.; Zevalkink, A.; Janek, J.; Zeier, W. G. Influence of Lattice Polarizability on the Ionic Conductivity in the Lithium Superionic Argyrodites Li 6 PS 5 X (X = Cl, Br, I). *J. Am. Chem. Soc.* **2017**, *139* (31), 10909–10918. https://doi.org/10.1021/jacs.7b06327.
- (9) Minafra, N.; Kraft, M. A.; Bernges, T.; Li, C.; Schlem, R.; Morgan, B. J.; Zeier, W. G. Local Charge Inhomogeneity and Lithium Distribution in the Superionic Argyrodites Li 6 PS 5 X (X = Cl, Br, I). *Inorg. Chem.* 2020, 59 (15), 11009–11019. https://doi.org/10.1021/acs.inorgchem.0c01504.
- (10) Gautam, A.; Sadowski, M.; Prinz, N.; Eickhoff, H.; Minafra, N.; Ghidiu, M.; Culver, S. P.; Albe, K.; Fässler, T. F.; Zobel, M.; Zeier, W. G. Rapid Crystallization and Kinetic Freezing of Site-Disorder in the Lithium Superionic Argyrodite Li 6 PS 5 Br. Chem. Mater. 2019, 31 (24), 10178–10185. https://doi.org/10.1021/acs.chemmater.9b03852.
- (11) Ohno, S.; Helm, B.; Fuchs, T.; Dewald, G.; Kraft, M. A.; Culver, S. P.; Senyshyn, A.; Zeier, W. G. Further Evidence for Energy Landscape Flattening in the Superionic Argyrodites Li6+ XP1- XMxS5I (M = Si, Ge, Sn). Chem. Mater. 2019, 31 (13), 4936–4944. https://doi.org/10.1021/acs.chemmater.9b01857.
- (12) Minafra, N.; Culver, S. P.; Krauskopf, T.; Senyshyn, A.; Zeier, W. G. Effect of Si Substitution on the Structural and Transport Properties of Superionic Li-Argyrodites. *J. Mater. Chem. A* **2018**, *6* (2), 645–651. https://doi.org/10.1039/C7TA08581H.
- (13) Žguns, P.; Yildiz, B. Strain Sensitivity of Li-Ion Conductuctivity in β-Li3PS4 Solid Electrolyte. PRX Energy 2022, 1 (2), 023003. https://doi.org/10.1103/PRXEnergy.1.023003.
- (14) Porz, L.; Klomp, A. J.; Fang, X.; Li, N.; Yildirim, C.; Detlefs, C.; Bruder, E.; Höfling, M.; Rheinheimer, W.; Patterson, E. A.; Gao, P.; Durst, K.; Nakamura, A.; Albe, K.; Simons, H.; Rödel, J. Dislocation-Toughened Ceramics. *Mater. Horizons* **2021**, *8* (5), 1528–1537. https://doi.org/10.1039/D0MH02033H.
- (15) Zheng, Y.; Slade, T. J.; Hu, L.; Tan, X. Y.; Luo, Y.; Luo, Z.-Z.; Xu, J.; Yan, Q.; Kanatzidis, M. G. Defect Engineering in Thermoelectric Materials: What Have We Learned? Chem. Soc. Rev. 2021, 50 (16), 9022–9054. https://doi.org/10.1039/D1CS00347J.

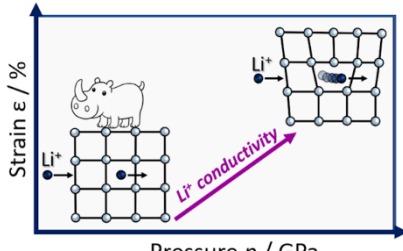
- (16) Hanus, R.; Agne, M. T.; Rettie, A. J. E.; Chen, Z.; Tan, G.; Chung, D. Y.; Kanatzidis, M. G.; Pei, Y.; Voorhees, P. W.; Snyder, G. J. Lattice Softening Significantly Reduces Thermal Conductivity and Leads to High Thermoelectric Efficiency. *Adv. Mater.* 2019, 31 (21), 1900108. https://doi.org/10.1002/adma.201900108.
- (17) Sun, L.; Marrocchelli, D.; Yildiz, B. Edge Dislocation Slows down Oxide Ion Diffusion in Doped CeO2 by Segregation of Charged Defects. *Nat. Commun.* **2015**, *6* (1), 6294. https://doi.org/10.1038/ncomms7294.
- (18) Legros, M.; Dehm, G.; Arzt, E.; Balk, T. J. Observation of Giant Diffusivity Along Dislocation Cores. *Science* (80-.). **2008**, 319 (5870), 1646–1649. https://doi.org/10.1126/science.1151771.
- (19) Kushima, A.; Yildiz, B. Oxygen Ion Diffusivity in Strained Yttria Stabilized Zirconia: Where Is the Fastest Strain? J. Mater. Chem. 2010, 20 (23), 4809–4819. https://doi.org/10.1039/c000259c.
- (20) Garcia-Barriocanal, J.; Rivera-Calzada, A.; Varela, M.; Sefrioui, Z.; Iborra, E.; Leon, C.; Pennycook, S. J.; Santamaria, J. Colossal Ionic Conductivity at Interfaces of Epitaxial ZrO 2:Y2O3/SrTiO3 Heterostructures. *Science (80-.).* **2008**, *321* (5889), 676–680. https://doi.org/10.1126/science.1156393.
- (21) Kang, B.; Ceder, G. Battery Materials for Ultrafast Charging and Discharging. *Nature* **2009**, *458* (7235), 190–193. https://doi.org/10.1038/nature07853.
- (22) Zhou, C.; Lee, Y. K.; Cha, J.; Yoo, B.; Cho, S.-P.; Hyeon, T.; Chung, I. Defect Engineering for High-Performance n-Type PbSe Thermoelectrics. *J. Am. Chem. Soc.* **2018**, *140* (29), 9282–9290. https://doi.org/10.1021/jacs.8b05741.
- (23) Adamczyk, J. M.; Gomes, L. C.; Qu, J.; Rome, G. A.; Baumann, S. M.; Ertekin, E.; Toberer, E. S. Native Defect Engineering in CuInTe2. *Chem. Mater.* **2021**, *33* (1), 359–369. https://doi.org/10.1021/acs.chemmater.0c04041.
- (24) Aydin, H.; Korte, C.; Rohnke, M.; Janek, J. Oxygen Tracer Diffusion along Interfaces of Strained Y2O 3/YSZ Multilayers. *Phys. Chem. Chem. Phys.* **2013**, *15* (6), 1944–1955. https://doi.org/10.1039/c2cp43231e.
- (25) Otsuka, K.; Kuwabara, A.; Nakamura, A.; Yamamoto, T.; Matsunaga, K.; Ikuhara, Y. Dislocation-Enhanced Ionic Conductivity of Yttria-Stabilized Zirconia. *Appl. Phys. Lett.* **2003**, *82* (6), 877–879. https://doi.org/10.1063/1.1544440.
- (26) Schneider, C.; Schmidt, C. P.; Neumann, A.; Clausnitzer, M.; Sadowski, M.; Harm, S.; Meier, C.; Danner, T.; Albe, K.; Latz, A.; Wall, W. A.; Lotsch, B. V. Effect of Particle Size and Pressure on the Transport Properties of the Fast Ion Conductor t -Li 7 SiPS 8. Adv. Energy Mater. 2023, 13 (15). https://doi.org/10.1002/aenm.202203873.
- (27) Dewald, G. F.; Ohno, S.; Hering, J. G. C.; Janek, J.; Zeier, W. G. Analysis of Charge Carrier Transport Toward Optimized Cathode Composites for All-Solid-State Li–S Batteries. *Batter. Supercaps* 2021, 4 (1), 183–194. https://doi.org/10.1002/batt.202000194.
- (28) Dewald, G. F.; Ohno, S.; Kraft, M. A.; Koerver, R.; Till, P.; Vargas-Barbosa, N. M.; Janek, J.; Zeier, W. G. Experimental Assessment of the Practical Oxidative Stability of Lithium Thiophosphate Solid Electrolytes. *Chem. Mater.* 2019, 31 (20), 8328–8337. https://doi.org/10.1021/acs.chemmater.9b01550.
- (29) Filik, J.; Ashton, A. W.; Chang, P. C. Y.; Chater, P. A.; Day, S. J.; Drakopoulos, M.;

- Gerring, M. W.; Hart, M. L.; Magdysyuk, O. V.; Michalik, S.; Smith, A.; Tang, C. C.; Terrill, N. J.; Wharmby, M. T.; Wilhelm, H. Processing Two-Dimensional X-Ray Diffraction and Small-Angle Scattering Data in DAWN 2. *J. Appl. Crystallogr.* **2017**, *50* (3), 959–966. https://doi.org/10.1107/S1600576717004708.
- (30) Coelho, A. A. TOPAS and TOPAS-Academic: An Optimization Program Integrating Computer Algebra and Crystallographic Objects Written in C++. *J. Appl. Crystallogr.* **2018**, *51* (1), 210–218. https://doi.org/10.1107/S1600576718000183.
- (31) Klotz, S.; Chervin, J.-C.; Munsch, P.; Le Marchand, G. Hydrostatic Limits of 11 Pressure Transmitting Media. *J. Phys. D. Appl. Phys.* **2009**, *42* (7), 075413. https://doi.org/10.1088/0022-3727/42/7/075413.
- (32) Angel, R. J.; Bujak, M.; Zhao, J.; Gatta, G. D.; Jacobsen, S. D. Effective Hydrostatic Limits of Pressure Media for High-Pressure Crystallographic Studies. *J. Appl. Crystallogr.* **2007**, *40* (1), 26–32. https://doi.org/10.1107/S0021889806045523.
- (33) Mao, H. K.; Xu, J.; Bell, P. M. Calibration of the Ruby Pressure Gauge to 800 Kbar under Quasi-Hydrostatic Conditions. *J. Geophys. Res.* **1986**, *91* (B5), 4673. https://doi.org/10.1029/jb091ib05p04673.
- (34) Syassen, K. Ruby under Pressure. *High Press. Res.* **2008**, *28* (2), 75–126. https://doi.org/10.1080/08957950802235640.
- (35) Huppertz, H. Multianvil High-Pressure / High-Temperature Synthesis in Solid State Chemistry. *Zeitschrift für Krist. Cryst. Mater.* **2004**, *219* (6), 330–338. https://doi.org/10.1524/zkri.219.6.330.34633.
- (36) Walker, D.; Carpenter, M. A.; Hitch, C. M. Some Simplifications to Multianvil Devices for High Pressure Experiments. *Am. Mineral.* **1990**, *75* (9–10), 1020–1028.
- (37) Walker, D. Lubrication, Gasketing, and Precision in Multianvil Experiments. *Am. Mineral.* **1991**, *76*, 1092–1100.
- (38) Williamson, G. .; Hall, W. . X-Ray Line Broadening from Filed Aluminium and Wolfram. *Acta Metall.* **1953**, *1* (1), 22–31. https://doi.org/10.1016/0001-6160(53)90006-6.
- (39) Chen, Z.; Jian, Z.; Li, W.; Chang, Y.; Ge, B.; Hanus, R.; Yang, J.; Chen, Y.; Huang, M.; Snyder, G. J.; Pei, Y. Lattice Dislocations Enhancing Thermoelectric PbTe in Addition to Band Convergence. *Adv. Mater.* **2017**, *29* (23), 1606768. https://doi.org/10.1002/adma.201606768.
- (40) Christensen, S.; Bindzus, N.; Sist, M.; Takata, M.; Iversen, B. B. Structural Disorder, Anisotropic Micro-Strain and Cation Vacancies in Thermo-Electric Lead Chalcogenides. *Phys. Chem. Chem. Phys.* 2016, 18 (23), 15874–15883. https://doi.org/10.1039/C6CP01730D.
- (41) Stephens, P. W. Phenomenological Model of Anisotropic Peak Broadening in Powder Diffraction. *J. Appl. Crystallogr.* **1999**, *32* (2), 281–289. https://doi.org/10.1107/S0021889898006001.
- (42) Besson, J. M.; Nelmes, R. J.; Hamel, G.; Loveday, J. S.; Weill, G.; Hull, S. Neutron Powder Diffraction above 10 GPa. *Phys. B Condens. Matter* **1992**, *180–181* (PART 2), 907–910. https://doi.org/10.1016/0921-4526(92)90505-M.
- (43) Klotz, S.; Hamel, G.; Frelat, J. A New Type of Compact Large-Capacity Press for Neutron and X-Ray Scattering. *High Press. Res.* **2004**, *24* (1), 219–223.

- https://doi.org/10.1080/08957950410001661963.
- (44) Sidhu, S. S.; Heaton, L.; Zauberis, D. D.; Campos, F. P. Neutron Diffraction Study of Titanium-Zirconium System. *J. Appl. Phys.* **1956**, *27* (9), 1040–1042. https://doi.org/10.1063/1.1722538.
- (45) Arnold, O.; Bilheux, J. C.; Borreguero, J. M.; Buts, A.; Campbell, S. I.; Chapon, L.; Doucet, M.; Draper, N.; Ferraz Leal, R.; Gigg, M. A.; Lynch, V. E.; Markvardsen, A.; Mikkelson, D. J.; Mikkelson, R. L.; Miller, R.; Palmen, K.; Parker, P.; Passos, G.; Perring, T. G.; Peterson, P. F.; Ren, S.; Reuter, M. A.; Savici, A. T.; Taylor, J. W.; Taylor, R. J.; Tolchenov, R.; Zhou, W.; Zikovsky, J. Mantid—Data Analysis and Visualization Package for Neutron Scattering and <math Altimg="si0002.Gif" Overflow="scroll"> <mi Mathvariant="normal">μ</Mi> </Math> SR Experiments. Nucl. Instruments Methods Phys. Res. Sect. A Accel. Spectrometers, Detect. Assoc. Equip. 2014, 764, 156–166. https://doi.org/10.1016/j.nima.2014.07.029.
- (46) Juhás, P.; Davis, T.; Farrow, C. L.; Billinge, S. J. L. PDFgetX3: A Rapid and Highly Automatable Program for Processing Powder Diffraction Data into Total Scattering Pair Distribution Functions. J. Appl. Crystallogr. 2013, 46 (2), 560–566. https://doi.org/10.1107/S0021889813005190.
- (47) Wankmiller, B.; Hansen, M. R. Observation of Li+ Jumps in Solid Inorganic Electrolytes over a Broad Dynamical Range: A Case Study of the Lithium Phosphidosilicates Li8SiP4 and Li14SiP6. *J. Magn. Reson. Open* **2023**, *14*–*15* (12), 100098. https://doi.org/10.1016/j.jmro.2023.100098.
- (48) Raiford, D. S.; Fisk, C. L.; Becker, E. D. Calibration of Methanol and Ethylene Glycol Nuclear Magnetic Resonance Thermometers. *Anal. Chem.* **1979**, *51* (12), 2050–2051. https://doi.org/10.1021/ac50048a040.
- (49) Thandavan, T. M. K.; Gani, S. M. A.; Wong, C. S.; Nor, R. M. Evaluation of Williamson–Hall Strain and Stress Distribution in ZnO Nanowires Prepared Using Aliphatic Alcohol. *J. Nondestruct. Eval.* **2015**, *34* (2), 14. https://doi.org/10.1007/s10921-015-0286-8.
- (50) Deiseroth, H.-J.; Kong, S.-T.; Eckert, H.; Vannahme, J.; Reiner, C.; Zaiß, T.; Schlosser, M. Li6PS5X: A Class of Crystalline Li-Rich Solids With an Unusually High Li+ Mobility. *Angew. Chemie Int. Ed.* **2008**, *47* (4), 755–758. https://doi.org/10.1002/anie.200703900.
- (51) Ungár, T.; Ott, S.; Sanders, P. .; Borbély, A.; Weertman, J. . Dislocations, Grain Size and Planar Faults in Nanostructured Copper Determined by High Resolution X-Ray Diffraction and a New Procedure of Peak Profile Analysis. *Acta Mater.* **1998**, *46* (10), 3693–3699. https://doi.org/10.1016/S1359-6454(98)00001-9.
- (52) Ungár, T.; Borbély, A. The Effect of Dislocation Contrast on X-Ray Line Broadening: A New Approach to Line Profile Analysis. Appl. Phys. Lett. 1996, 69 (21), 3173–3175. https://doi.org/10.1063/1.117951.
- (53) Tong, X.; Zhang, H.; Li, D. Y. Effect of Annealing Treatment on Mechanical Properties of Nanocrystalline α -Iron: An Atomistic Study. *Sci. Rep.* **2015**, *5* (1), 8459. https://doi.org/10.1038/srep08459.
- (54) Hendriks, T. A.; Lange, M. A.; Kiens, E. M.; Baeumer, C.; Zeier, W. G. Balancing Partial Ionic and Electronic Transport for Optimized Cathode Utilization of High-Voltage LiMn 2 O 4 /Li 3 InCl 6 Solid-State Batteries. *Batter. Supercaps* 2023, 6 (4). https://doi.org/10.1002/batt.202200544.

- (55) Minnmann, P.; Quillman, L.; Burkhardt, S.; Richter, F. H.; Janek, J. Editors' Choice— Quantifying the Impact of Charge Transport Bottlenecks in Composite Cathodes of All-Solid-State Batteries. J. Electrochem. Soc. 2021, 168 (4), 040537. https://doi.org/10.1149/1945-7111/abf8d7.
- (56) de Biasi, L.; Schwarz, B.; Brezesinski, T.; Hartmann, P.; Janek, J.; Ehrenberg, H. Chemical, Structural, and Electronic Aspects of Formation and Degradation Behavior on Different Length Scales of Ni-Rich NCM and Li-Rich HE-NCM Cathode Materials in Li-lon Batteries. Adv. Mater. 2019, 31 (26). https://doi.org/10.1002/adma.201900985.
- (57) Koerver, R.; Zhang, W.; de Biasi, L.; Schweidler, S.; Kondrakov, A. O.; Kolling, S.; Brezesinski, T.; Hartmann, P.; Zeier, W. G.; Janek, J. Chemo-Mechanical Expansion of Lithium Electrode Materials – on the Route to Mechanically Optimized All-Solid-State Batteries. *Energy Environ. Sci.* 2018, 11 (8), 2142–2158. https://doi.org/10.1039/C8EE00907D.
- (58) Zhang, W.; Weber, D. A.; Weigand, H.; Arlt, T.; Manke, I.; Schröder, D.; Koerver, R.; Leichtweiss, T.; Hartmann, P.; Zeier, W. G.; Janek, J. Interfacial Processes and Influence of Composite Cathode Microstructure Controlling the Performance of All-Solid-State Lithium Batteries. ACS Appl. Mater. Interfaces 2017, 9 (21), 17835–17845. https://doi.org/10.1021/acsami.7b01137.
- (59) Schlautmann, E.; Weiß, A.; Maus, O.; Ketter, L.; Rana, M.; Puls, S.; Nickel, V.; Gabbey, C.; Hartnig, C.; Bielefeld, A.; Zeier, W. G. Impact of the Solid Electrolyte Particle Size Distribution in Sulfide-Based Solid-State Battery Composites. *Adv. Energy Mater.* 2023, 2302309, 1–9. https://doi.org/10.1002/aenm.202302309.

For table of contents only



Pressure p / GPa